J Braz. Soc. Mech. Sci. Eng. (2017) 39:645–659
DOI 10.1007/s40430-016-0598-3

TECHNICAL PAPER

An osteosynthesis plate analytical model

Paulo Pedro Kenedi[1,2] · **Lucas Lisboa Vignoli**[3]

Received: 29 September 2015 / Accepted: 5 July 2016 / Published online: 19 July 2016

Abstract Osteosynthesis plates are used to fix broken bones to help the healing process consolidation. It consists in fixing a plate on a long-bone external surface with screws, sharing forces, and moments between bone and plate. In this paper, a straight osteosynthesis plate is analyzed using an analytical bi-material model, based on mechanics of solids, to estimate the mechanical stress distributions at plate medial cross sections. The analytical model results show good performance in comparison with the commercial finite-element software used as reference.

Keywords Osteosynthesis plate · Stress analysis · Analytical model · Finite-element model

1 Introduction

The utilization of osteosynthesis plates, for now on called just plates, in long-bone surgery has undergone enormous developments. The bone material was analyzed by authors as Doblaré et al. [8], which introduces bone biology, bone mechanical properties, mechanisms of bone fracture, and comments about a tentative bone fracture criteria, models fractures, and fracture healing. The bone failure theories were accessed, for instance, by Keyak and Rosi [20], which propose a comparative study, via finite-element method, between experimental fracture load of frozen human femurs and the application of failure theories of ductile and fragile materials. Very interesting research was done in plate clinical applications by Kubiak et al. [21], which proposes to review the history of locked plates and the current recommendations for the use of those devices and look toward future trends in the clinical application of locked plates. Rockwood and Green [25] made a very complete treatise about plate applications, including surgical instructions and Frigg [14], based on clinical experience with PC-Fix, and indicated the advantages of bridging plate with the utilization of internal fixator in comparison with the conventional plate procedures.

Numerical models were proposed by Rudman et al. [26] to access muscle-bone interactions, through the utilization of a 2D F.E. model, by studying the influence of tendons on stress distribution in the proximal femur. Duda et al. [9] used a finite-element model to demonstrate the influence of muscle forces in human femur strain distribution, showing that the bone loaded with all the thigh muscles experienced a somewhat homogeneous strain distribution.

Many published research of bone and/or plate deal with experimental research. Femoral implants are the subject of Bergmann et al. [3] that measured the hip contact forces through the utilization of instrumented femoral implants. Tung-Wu et al. [34] did experiments on two patients with custom-made instrumented massive proximal femoral prostheses implanted after tumor resection. In vivo axial forces transmitted along the prostheses were telemetered during

Technical Editor: Estevam Las Casas.

✉ Paulo Pedro Kenedi
paulo.kenedi@cefet-rj.br

Lucas Lisboa Vignoli
lucas.lvig@gmail.com

[1] PPEMM-Programa de Pós-Graduação em Engenharia Mecânica e Tecnologia de Materiais, CEFET/RJ, Av. Maracanã, 229, Maracanã, RJ CEP 20271-110, Brazil

[2] DEMEC-Departamento de Engenharia Mecânica, CEFET/RJ, Av. Maracanã, 229, Maracanã, RJ CEP 20271-110, Brazil

[3] COPPE-Department of Mechanical Engineering, Center for Nonlinear Mechanics, Universidade Federal do Rio de Janeiro, PO Box 68.503, 21.941.972 Rio de Janeiro, Brazil

level walking, single and double-leg stance, and isometric exercises of the hip muscles. It was concluded that appropriate simulation of muscle forces was important in the experimental or theoretical studies of load transmission along bones.

The plate performance was accessed by Goswami et al. [16], which experimentally analyzes various combinations of locking and non-locking screws under simultaneous axial and torsional loadings to determine the optimal hybrid locking plate-screw construct in a fourth generation composite femur. Talbot et al. [30] studied the fixation of long-bone segmental defects through the utilization of three constructs: lateral locking plate; lateral non-locking plate and medial allograft strut; and lateral non-locking plate and intramedullary fibula allograft. Ahmad et al. [1] did in vitro investigation of the mechanical stability of a locking compression plate (LCP) construct in a simulated diaphysis fracture of the humerus at increasing distances between the plate and bone. Cordey et al. [5] did an experimental quantification of the importance of the screws bending stiffness and the friction between plate and bone in the plate performance.

The bone surface strains were measured by Simões et al. [27] who studied the influence of muscle action and a horizontally constrained femoral head on the strain distribution within the intact femur for three loading configurations: joint reaction force only, joint reaction force plus abductors, and joint reaction force plus the abductors, vastus lateralis, and iliopsoas, with the use of uniaxial strain gauges placed on the medial, lateral, anterior, and posterior aspects of the proximal femur. Cristofolini et al. [7] studied experimentally the bone surface strains using a custom designed jig to measure external surface strains at proximal human femur, generated by the simulated loading of each thigh muscle, resulting in a great variability of strain responses as a function of the muscles or group of muscles selected.

Other experimental methods were used by Edwards et al. [13] stating that the external muscular loading of long bones is an important factor in determining stress and strain distributions at the external surface of cortical bone. Muscle forces are estimated by the utilization of force platform and motion capture data through static optimization in conjunction with a SIMM musculoskeletal model. Sommers et al. [29] develop a mechanical surrogate model for osteoporotic diaphysis bone, to replicate torsional rigidity and strength, bending rigidity and strength, and screw pull-out strength. Experimental tests indicate good agreement between surrogate long-bone models and cadaveric femura.

Duda et al. [11], in an experimental study, determine that anatomical variability significantly influences the results of biomechanical analyses, particularly the moment arm of the various thigh muscles, and conclude that some muscle moment arms are very sensitive to the anatomical situation, such as gluteus maximus and m. rectus femoris, whereas others are not, such as gluteus medius and m. gastrocnemi.

Analytical models are accessed by Kenedi and Riagusoff [18] through the utilization of mechanics of solids theory, to model the stress distribution at a medial external bone surface path. Both cortical and trabecular bone tissues were recognized, and the medial bone cross sections were model as circular or as elliptical. The principal stress, with respective angles, results were accessed and compared with an F.E. model, used as reference. Ramos and Simões [24] used the well-known Castigliano theorem to access stresses and displacements of a femur modeled as a straight column and an arch. Duda et al. [10] represent a system in equilibrium through the forces exerted together by the soft and hard tissues. In addition, to improve the understanding of femoral loading, a three-dimensional model was developed taking into account thigh muscles, body weight and contact forces at the hip, patello-femoral, and knee joints. Raftopoulos and Qassem [23] proposed two interesting analytical models: one with straight and homogeneous beams and other with curved and composite beams. Gdoutos et al. [15] did an interesting review of what other researchers have done in stress analysis of human femurs. Toridis [33] in an early work proposed an analytical model of human femur stress analysis taking into account both cortical and trabecular bones tissues at an arbitrary bone cross section.

In this work, an analytic model, based on mechanics of solids, is proposed as a development of Kenedi and Vignoli [19], to relate external forces acting at a human femur head with the internal loads acting at combined set of bone and plate cross sections and to obtain a better understanding of internal loadings shares between bone and plate at a diaphysis long-bone central region and, consequently, its cross sections stress distributions. A finite-element model is also provided, as a reference, including the presence of screws and contact stresses.

Figure 1a shows a model of a real human femur bone with femur's head load with a plate installed on a diaphysis femur bone external surface region. The external forces used in this model were adapted from of Taylor et al. [31] fourth load case of a human femur's head. These forces are named : Joint Reaction, at point *A;* Abductors, at point *B*; Ilioopsoas, at point *C*, and, Ilio-Tibial Tract, at point *D*, which are a significant simplification of real human's femur bone external loading (see Bitsakos et al. [4] for a more complete muscle loading case description). Figure 1b shows bone/plates at a coronal plane in detail. The plate is fixed at the lateral side of the central part of the femur diaphysis through the utilization of six screws. In addition, it is possible to recognize that the bone irregular external surface generates irregular distances between plate and bone, which could lead to irregular contacts between them.

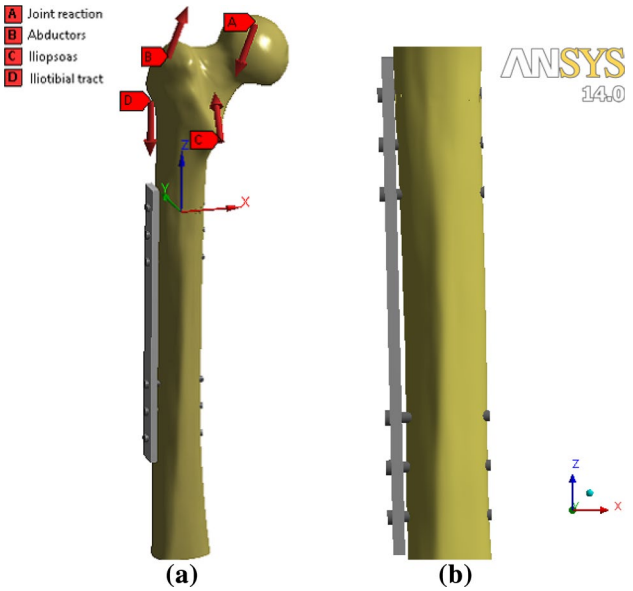

Fig. 1 Human femur with a plate at diaphysis region (coronal plane): **a** general view and **b** detailed view

Note that relative position between plate and bone, for instance, the plate parallelism with bone to z axis, varies from bone to bone, which adds a certain degree of geometric variability to the definition of plate-effective position.

At next item, the analytical model is proposed in detail.

2 Analytical model

In this section, an analytical model is proposed, based on mechanics of solids, to describe the load share between bone and plate, with the ultimate objective of estimating the stress distribution at plate diaphysis cross sections.

To implement the analytical model, few hypotheses have to be imposed as: the external loading is represented by four static forces that are concentrated at femur's head, as already mentioned at the previous section; no bone side ligaments are recognized; and the bone and plate cross sections are assumed to be, respectively, hollow circular (with constant thickness wall) and rectangular (with or without a screw hole). In addition, the bone tissue is assumed to be cortical and the plate material is made of stainless steel, both modeled as isotropic, see Kenedi and Vignoli [19].

To estimate the load acting at a plate medial cross section, the load sharing between bone and plate must be calculated. To facilitate mathematical manipulation, the static forces, applied at the femur's head, are represented by numerical indices: Joint Reaction force (P_1), Abductor force (P_2), Iliopsoas force (P_3), and Iliotibial Tract force (P_4). The forces P_i and the moments M_i are calculated at the combined cross-sectional centroid; and the distances d_i between forces application points and the combined cross-sectional centroid can be written as

$$P_i = P_{i,x_g}\vec{i} + P_{i,y_g}\vec{j} + P_{i,z_g}\vec{k} \quad d_i = d_{i,x_g}\vec{i} + d_{i,y_g}\vec{j} + d_{i,z_g}\vec{k} \tag{1}$$

$$\begin{pmatrix} M_{i,x_g} \\ M_{i,y_g} \\ M_{i,z_g} \end{pmatrix} = \begin{pmatrix} d_{i,y_g}P_{i,z_g} - d_{i,z_g}P_{i,y_g} \\ d_{i,z_g}P_{i,x_g} - d_{i,x_g}P_{i,z_g} \\ d_{i,x_g}P_{i,y_g} - d_{i,y_g}P_{i,x_g} \end{pmatrix} \tag{2}$$

where the indices i vary from 1 to 4, g subscripts are referenced to global system coordinates. $\vec{i}$, $\vec{j}$, and $\vec{k}$ are unit vectors. P_{i,x_g},P_{i,y_g},P_{i,z_g} and M_{i,x_g},M_{i,y_g},M_{i,z_g} are, respectively, the components of each global force and global moment at the combined cross-sectional centroid. Note that the combined cross section is the set of plate and bone cross sections, as shown in Fig. 2a. The expressions (3) and (4) show the components global force and global moment summation:

$$N^g = \sum_{i=1}^{4} P_{i,z_g} \quad V_x^g = \sum_{i=1}^{4} P_{i,x_g} \quad V_y^g = \sum_{i=1}^{4} P_{i,y_g} \tag{3}$$

$$M_x^g = \sum_{i=1}^{4} M_{i,x_g} \quad M_y^g = \sum_{i=1}^{4} M_{i,y_g} \quad T^g = \sum_{i=1}^{4} M_{i,z_g} \tag{4}$$

where N^g, V_x^g, V_y^g and M_x^g, M_y^g, and T^g are, respectively, the global force and global moment summation at a combined cross-sectional centroid. Figure 2a shows plate and bone cross sections, with the plate in a generic angular position θ_z, and Fig. 2b shows the plate at angular position $\theta_z = 180°$, which was used in this work example.

Where B and H are, respectively, plate width and thickness, D_o and D_i are, respectively, bone model external and internal diameters. Beyond the main dimensions, Fig. 2a, b shows the position of bone centroid, plate centroid (both marked with a cross), and the combined cross-sectional centroid (where the local axis origin is positioned).

As already commented at the previous section, the plate effective position has some variability, so the plate centroid position can be shifted at both x and y local axis directions to accommodate such deviations. To describe the relations between the plate cross-sectional centroid, the bone cross-sectional centroid, and the combined cross-sectional centroid, four variables were created: m, n, s, and t. The variables m and n are, respectively, the distances from bone centroid and from plate centroid to the combined cross section in local y axis direction. The variables s and t are, respectively, the distances from bone centroid and from plate centroid to the combined cross section in local x axis direction. Figure 2b also shows the distances used to estimate the combined cross-sectional centroid for $\theta_z = 180°$, in which expressions are shown in (5) and (6), Crandall et al. [6]:

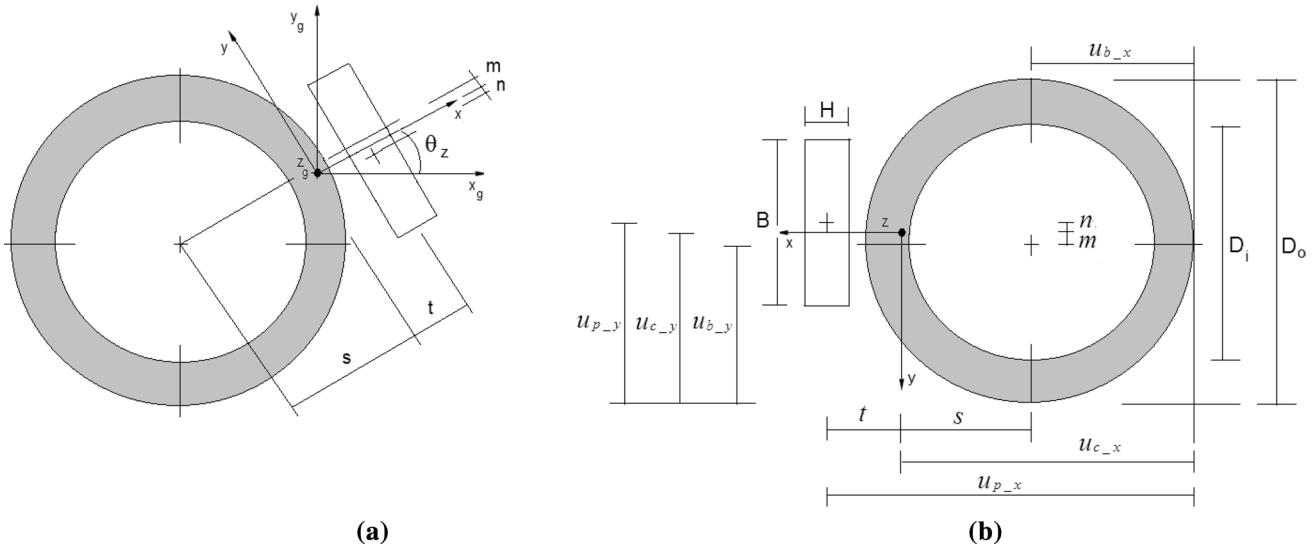

Fig. 2 Plate and bone cross sections main dimensions. **a** Plate at a generic angular position θ_z and **b** plate at $\theta_z = 180°$

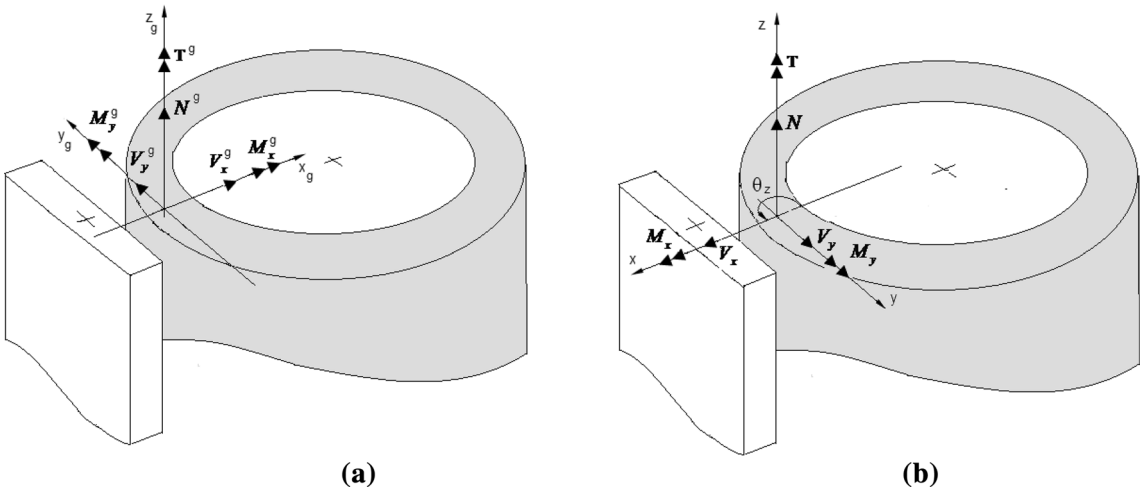

Fig. 3 Combined cross section: **a** global force and moment summation, **b** local force and moment summation

$$u_{c\_x} = \frac{A^b E^b u_{b\_x} + A^p E^p u_{p\_x}}{A^b E^b + A^p E^p} \quad u_{c\_y} = \frac{A^b E^b u_{b\_y} + A^p E^p u_{p\_y}}{A^b E^b + A^p E^p} \tag{5}$$

$$\begin{aligned} m &= u_{b\_y} - u_{c\_y} \quad n = u_{p\_y} - u_{c\_y} \\ s &= u_{b\_x} - u_{c\_x} \quad t = u_{p\_x} - u_{c\_x} \end{aligned} \tag{6}$$

where b, c, and p refer, respectively, to bone, combined, and plate. A is a cross-sectional area, E is a modulus of elasticity, and u is a position. Note that u_{b_x}, u_{b_y}, u_{p_x}, and u_{p_y} are real positions to be obtained from bone/plate cross sections. Figure 3a shows the forces and moments summation vectors of expressions (3) and (4) at combined centroid cross section in global coordinates, and Fig. 3b shows the force and moment summation vectors in local coordinates, in which expressions are shown, in a compact form, in (7).

Expression (7) shows the force and moment summations in local coordinates, as shown in Fig. 3b:

$$\begin{bmatrix} V_x \\ V_y \\ N \end{bmatrix} = \Theta_z \begin{bmatrix} V_x^g \\ V_y^g \\ N^g \end{bmatrix} \quad \begin{bmatrix} M_x \\ M_y \\ T \end{bmatrix} = \Theta_z \begin{bmatrix} M_x^g \\ M_y^g \\ T^g \end{bmatrix} \tag{7}$$

where V_x, V_y, N, and M_x, M_y, and T are, respectively, the local force and moment summation in local coordinates, and Θ_z is the rotation transformation matrix around z axis, which is available in Appendix Table 8.

In the next section, the load sharing between bone and plate is proposed.

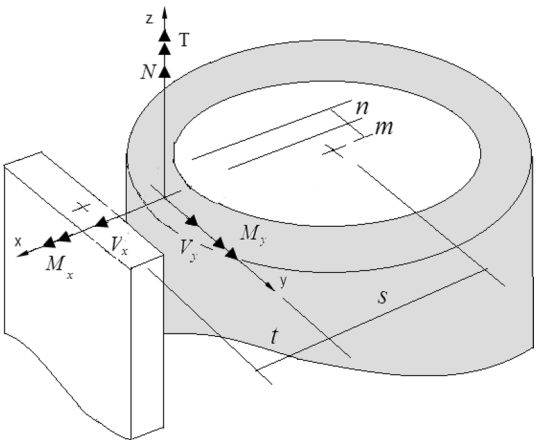

Fig. 4 Force and moments at combined cross section at local coordinates and the distance variables: *m*, *n*, *s*, and *t*

2.1 The load sharing

One of the alternatives to deal with a bi-material problem using mechanics of solids is to suppose that the problem can be reduced to two different material beams in parallel configuration, as in Crandall et al. [6]. The plate is firmly attached to the bone external surface by screws, as can be seen in Fig. 1b. For analytical model purposes, it is important to stablish how plate and bone cross-sectional responses to the load input.

Figure 4 shows the V_x, V_y, N, M_x, M_y, and T components at combined cross section and the distance variables: m, n, s, and t.

Although the plate isn't in entirely vertical position, it is supposed that the deviation is quite small, and for the analytical model purposes, its effects are neglected.

The load share expressions, for axial force N in Fig. 4, are estimated as

$$N^p = \left(\frac{1}{1+(a^*e^*)^{-1}}\right)N \quad N^b = \left(\frac{1}{1+a^*e^*}\right)N \tag{8}$$

where a^* and e^* are, respectively, the area ratio and the modulus of elasticity ratio, in which expressions are available in Appendix Table 8. The load share expressions, for shear forces V_x and V_y in Fig. 4, are estimated as

$$V_x^p = \left(\frac{1}{1+\left(e^*s_x^*\right)^{-1}}\right)V_x \quad V_x^b = \left(\frac{1}{1+e^*s_x^*}\right)V_x$$
$$V_y^p = \left(\frac{1}{1+\left(e^*s_y^*\right)^{-1}}\right)V_y \quad V_y^b = \left(\frac{1}{1+e^*s_y^*}\right)V_y \tag{9}$$

$$I_x^{b*} = I_x^b + A^b m^2 \quad I_x^{p*} = I_x^p + A^p n^2$$
$$I_y^{b*} = I_y^b + A^b s^2 \quad I_y^{p*} = I_y^p + A^p t^2 \tag{10}$$

where, s_x^* and s_y^* are, respectively, area moment of inertia ratio (relative to x axis) and area moment of inertia ratio (relative to y axis) of combined cross section, in which expressions are available in Appendix Table 8. Note that expressions (10) represents the use of the parallel axis theorem [6] to take into account the distances m and s of the bone centroid and the distances n and t of the plate centroid, and both relatives to the combined cross-sectional centroid.

In the next section, stress distribution in two different plate cross sections is estimated.

2.2 Plate cross-sectional stress distribution

In this item, the plate cross-sectional distribution is estimated for a diaphysis plate cross section without hole, named for now on *full*, and for a diaphysis plate cross section with a hole of diameter d, named for now on *hollow*, as shown in Fig. 11a, by the following expressions, from (11) to (21), with the aid of Appendix Tables 7 and 8.

The plate axial stress distribution $\sigma^p_{z_{axial}}$ can be estimated as, Crandall et al. [6]:

$$\sigma^p_{z_{axial}} = C_1\frac{N^p}{A^p} \quad C_1 = \begin{vmatrix} 1 & \text{full} \\ K_{t\_axial} & \text{hollow} \end{vmatrix}. \tag{11}$$

The A^p expression depends on the cross section being full or hollow, as shown in Appendix Table 7. The 2D stress concentration factor (SCF) of the hole, at extremities of lines 5a and 5b in Fig. 11, in y axis direction, is K_{t_axial} [37]:

$$K_{t\_axial} = 3.00 - 3.13\left(\frac{d}{B}\right) + 3.66\left(\frac{d}{B}\right)^2 - 1.53\left(\frac{d}{B}\right)^3. \tag{12}$$

Note that although K_{t_axial} correspond to two punctual values (diametrically opposed at each plate surface), it is supposed, as an upper bound approximation, that K_{t_axial} is maintained through all extension of lines 5a and 5b in Fig. 11.

The plate bending out of plane stress distribution $\sigma^p_{z_{bend}}(x)$ and the plate bending in plane stress distribution $\sigma^p_{z_{bend}}(y)$ can be estimated as, Crandall et al. [6]:

$$\sigma^p_{z_{bend}}(x) = -\frac{x}{\left(1+\left(e^*s_y^*\right)^{-1}\right)}M_y \quad \text{for } -H/2+t \le x \le H/2+t \tag{13}$$

$$\sigma^p_{z_{bend}}(y) = \frac{y}{\left(1+\left(e^* s^*_x\right)^{-1}\right)} M_x \quad -B/2-n \le y \le B/2-n \quad \text{for full } -B/2-n \le y \le -d/2-n \quad \text{and } d/2-n \le y \le B/2-n \quad \text{for hollow.} \tag{14}$$

Note that s^*_x and s^*_y expressions depend if the cross sections are full or hollow, as shown in Appendix Table 7. The plate transverse shears stresses $\tau^p_{zx_{ts}}(x)$ and $\tau^p_{zy_{ts}}(y)$ can be estimated as, Crandall et al. [6]:

$$\tau^p_{zx_{ts}}(x) = \frac{V^p_x Q^p_y(x)}{\left(1+\left(e^* s^*_y\right)^{-1}\right) B} \quad \text{for } -H/2+t \le x \le H/2+t \tag{15}$$

$$\tau^p_{zy_{ts}}(y) = \frac{V^p_y Q^p_x(y)}{\left(1+\left(e^* s^*_y\right)^{-1}\right) H} \quad \text{for } -B/2-n \le y \le B/2-n. \tag{16}$$

Where $Q^p_x(y)$ and $Q^p_y(x)$ are the first moment of area relative, respectively, to x and y axes, and have different expressions for full or hollow cross sections, as shown in Appendix Table 7. Because the range of expressions (15) and (16) is relative to the combined cross-sectional centroid, they do not predict null stresses at external plate surfaces, as they should, which can be considered a limitation of this model. As stress values of expressions (15) and (16) present small values, the overall effect is not significative (principally near of external plate surfaces) and can be neglected.

The torsional load share between plate and bone is estimated supposing a parallel configuration [28, 32]:

$$k_p = \frac{1}{3} G^p B H^3 \left(1 - 0.63\frac{H}{B}\right)$$
$$k_b = G^b \pi \left(\frac{D_o^4 - D_i^4}{32}\right) \quad k_{eq} = k_b + k_p \tag{17}$$

where G is the shear modulus, k is the torsional stiffness, and the subscript eq is the abbreviation of equivalent. The effect of two different structures in parallel with an applied torque is discussed with more detail in [32]. The torsional stresses can be estimated as, Timoshenko and Goodier [32] and Ecsedi [12]:

$$\tau^p_{zx_t}(x,y) = -\frac{8G^p H}{\pi^2}\frac{T}{k_{eq}} \sum_{i=0}^{\infty} \left\{ \frac{(-1)^i}{(2i+1)^2} \left[\frac{\sinh\left(\frac{(2i+1)\pi}{H} y\right)}{\cosh\left(\frac{(2i+1)\pi}{H}\frac{B}{2}\right)} \right] \cos\left(\frac{(2i+1)\pi}{H} x\right) \right\} \tag{18}$$

$$\tau^p_{zy_t}(x,y) = G^p \frac{T}{k_{eq}} \left\{ 2x - \frac{8H}{\pi^2} \sum_{i=0}^{\infty} \left\{ \frac{(-1)^i}{(2i+1)^2} \left[\frac{\cosh\left(\frac{(2i+1)\pi}{H} y\right)}{\cosh\left(\frac{(2i+1)\pi}{H}\frac{B}{2}\right)} \right] \sin\left(\frac{(2i+1)\pi}{H} x\right) \right\} \right\}. \tag{19}$$

Note that the analytical model does not recognize the differences of stress distribution for plate transverse shear stresses and torsional stresses between full and hollow plate cross sections. It uses, for both cases, the cross-sectional stress distribution for full plate. As these shear stresses are an order of magnitude lower that the normal stresses, axial and bending, it is supposed that this model limitation do not disturb excessively the plate cross-sectional stress distribution. In addition, note that for the hollow cross section (with a screw hole), only the nominal axial stresses was multiplied by a stress concentration factor (SCF). For hollow plate cross-sectional geometry for bending, transverse shear, and torsional loadings, there is no SCF available in technical literature, as in [36, 37]. Nevertheless, see [38] for an interesting technical paper in this area. The sum of the stress distribution effects produced by each load at a diaphysis plate cross section can be estimated utilizing the von Mises criterion, as Crandall et al. [6]:

$$\sigma^p_z(x,y) = \sigma^p_{z_{axial}} + \sigma^p_{z_{bend}}(x,y) \quad \tau^p_{zx}(x,y) = \tau^p_{zx_{ts}}(x) + \tau^p_{zx_t}(x,y)$$
$$\tau^p_{zy}(x,y) = \tau^p_{zy_{ts}}(y) + \tau^p_{zy_t}(x,y) \tag{20}$$

$$\sigma_{vM}(x,y) = \left\{ \left(\sigma^p_z(x,y)\right)^2 + 3\left[\left(\tau^p_{zx}(x,y)\right)^2 + \left(\tau^p_{zy}(x,y)\right)^2 \right] \right\}^{\frac{1}{2}}. \tag{21}$$

To implement the analytical model expressions, from (1) to (21), a mathematical software as Mathcad or MATLAB must be used. In next section, the Numerical model is presented.

3 Numerical model

The numerical model was built up using the F.E. software ANSYS, to simulate the effects of muscles loads acting on the bone/plate set. In next item, a detailed description of geometry and mesh is given.

3.1 The geometry and meshing

Figure 5 shows the mesh used at many parts/regions of the numerical simulation. The bone head mesh was less refined

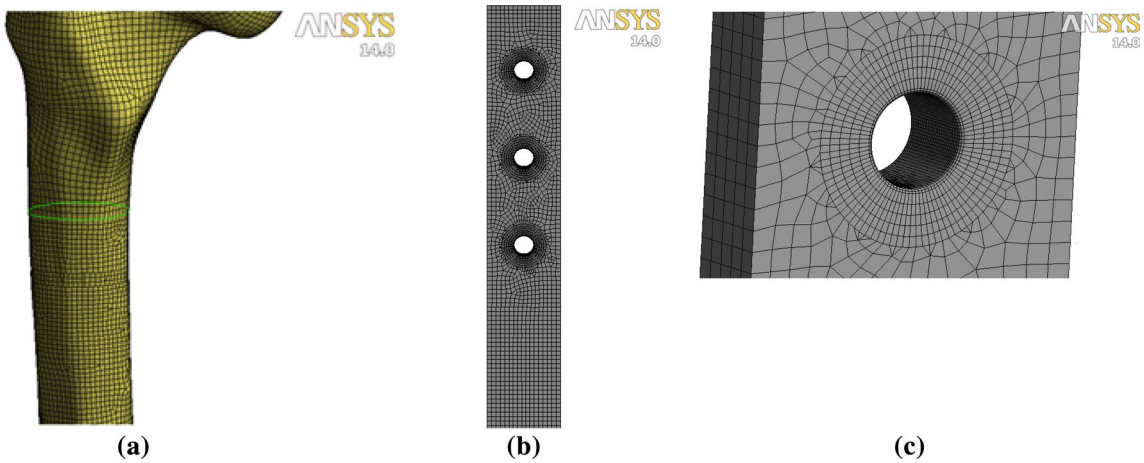

Fig. 5 Mesh: **a** Bone; **b** plate, and **c** pate hole in detail

than the diaphysis bone region, based on Vignoli and Kenedi [35] results. The green line shown in Fig. 5a limits these different mesh regions. The head region has an average element size of 2.5 mm, and the body region has the average element size of 2.0 mm. For both femur regions, because the irregular geometry, elements with midside nodes were adopted, SOLID186 and SOLID187. For the plate mesh, it was chosen simpler elements as SOLID285 and SOLID185, which not have midside nodes; therefore, the average element size decreases to 1 mm. A circular region was created concentric to each plate screw hole with 90 division along the circumference and 5 divisions in radial direction, as shown in Fig. 5b and c. The screw mesh used the elements SOLID285 and SOLID185 with 1.5 mm size, except at the external surface, where the bolt pretension is applied, which was used the element PRETS179 with 0.25 mm size. All the mesh dimensions, as well as the elements, were adopted after a convergence study to obtain a better convergence without an excessive computational cost. A total of 323,945 solid elements, 83,099 contact elements, and 424,471 nodes were used.

To simplify the contacts nomenclature, the following abbreviations were adopted: PS, BS, and PB for, respectively, plate/screw, bone/screw, and plate/bone contacts. The simulations were carried out using a few hypotheses with respect to contacts between parts: the BS and PS contacts do not allow separation neither slip on their surfaces, representing the screw thread. It was difficult to generate F.E. screw threads model, because it is quite irregular shape. In addition, it was hard to model the contact because penetration issues, and thus, a smooth surface was used. The MPC (Multi-Point Constraint) formulation was selected for the screw contacts, because it faster solution. As this formulation has some limitations, it only can be used for some specific contact definitions.

The PB contact is set as frictionless and the Pure Penalty was used because of convergence issues. All the contacts are defined as asymmetric. The following definition of contact/target bodies was used: for PS, the plate was the contact, because its finer mesh and the screw were the target; for BS, the bone was the contact and the screw was the target, because of its stiffer characteristic; and for PB, the plate was the contact and the bone was the target, because of its element sizes. For a more detailed description about contacts formulation applied in Ansys, see Lee [22].

The bolt preload is considered enough to fix the plate. The screw torque was set in 1 Nm, and the torque coefficient was set to 0.2. The simulation was executed in two load steps: on the first step, the bottom part of the bone was fixed and each bolt pretension was applied, at the second load step, the static forces acting on the femur head were applied. The numerical model was built up using the finite-element software ANSYS to simulate the effect of the muscles loads acting on the bone/plate set. Four external static forces applied at femur's head and proximal region (Fig. 1a). The distal part is considered fixed.

Figure 6 shows the femur in a sagital position with seven cross sections named from *a* to *g*. Note that six cross sections have screw hole and the medial one not.

Figure 6 shows many interesting aspects of bone cross sections. The most apparent is the huge cross-sectional variations, especially with respect to the outer diameter and thickness, whereas the internal diameter although alters its dimensions maintains a reasonable circular aspect. Another point that worth mentioning is that although the screw holes were done with the intention of maintaining them relatively centralized, in respect to each cross section, the overall results were rather decentralized. Note that only at central cross section *d* there is no screw hole.

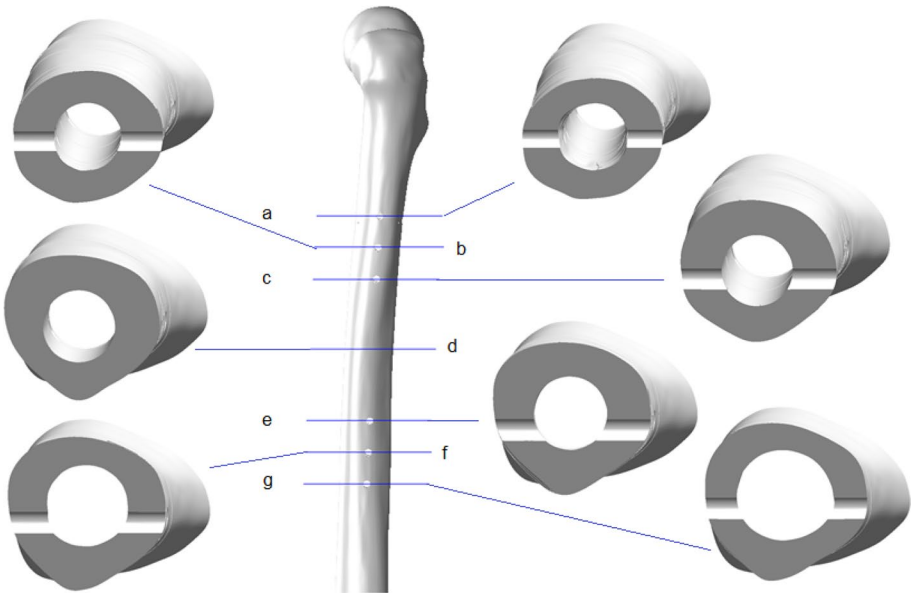

Fig. 6 Bone cross sections. Proximal: *a*, *b,* and *c*, Medial *d,* and Distal *e*, *f,* and *g*

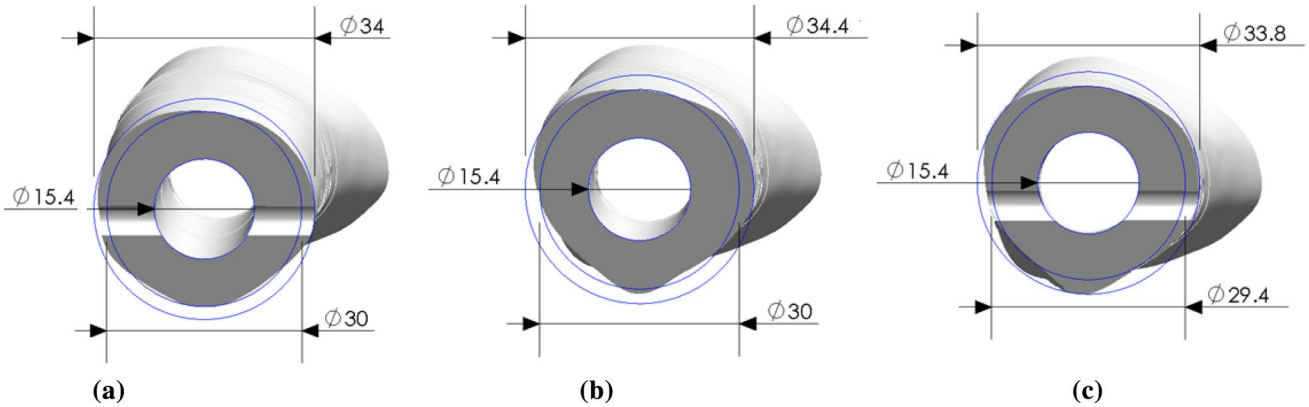

Fig. 7 Examples of bone cross sections: **a** proxinal (*c* in Fig. 6), **b** medial (*d* in Fig. 6), and **c** distal (*e* in Fig. 6)

Figure 7 shows three cross-sectional examples, one proximal, one medial, and one distal. As was already mentioned, there are huge dimensional variations between bone cross sections, principally at outer diameters and thicknesses. Therefore, it is very important to analytical model performance, to do the best possible regular pattern fit of a circle to the irregular pattern of the bone external diameters.

To meet the best possible circular fit to the outer diameter, two circular blue lines were plotted at each analyzed cross sections (note that the inner diameters are pretty circular). One blue circle is tangent to the inner point of outer cross-sectional diameter and the other is tangent to outer point of the outer cross-sectional diameter. The average diameter of these two blue lines of external diameter was chosen, after a geometrical analysis, as the best possible circular fit to a quite irregular bone real pattern. Figure 8 shows two real combined cross sections, with the centroids positions, used in the article example.

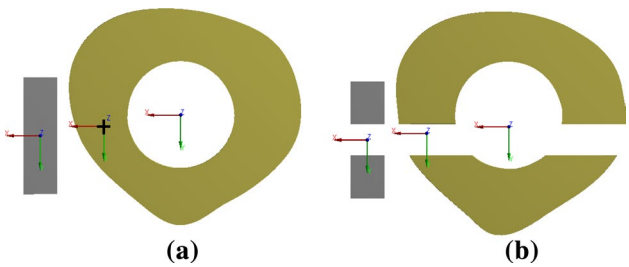

Fig. 8 Combined cross sections, with centroids positions for: **a** plate full (*d* in Fig. 6) and **b** plate hollow (*e* in Fig. 6)

The medial cross-sectional bone/plate (full) set, shown in Fig. 8a, corresponds to Fig. 6. at position *d*. A cross in Fig. 8a displays the origin of the coordinates. The medial

cross-sectional bone/plate (hollow) set, shown in Fig. 8b, corresponds to Fig. 6 at position *e*. Note that although the inner diameters are pretty circular, the outer diameters are not, resulting in an overall non-constant thickness patterns. In addition, the plate cross-sectional centroids have a significant shift in both *x* and *y* axes' directions in respect to each bone cross-sectional centroid. In next item, the data used in the article example were given.

3.2 The example data

The next six tables show geometrical, material, and loading inputs necessary to do the article example for both analytical and F.E. models (Table 1).

Note that the outer bone diameter D_o was chosen after a geometrical analysis of the best possible circular fit to a quite irregular bone real patterns, as shown in Fig. 7. The *B* and *H* plate dimensions were obtained from [2] (Tables 2, 3, 4, 5, 6).

The points of application of forces were adapted from a fourth load case of a human femur's head of Taylor et al. [31].

The centroids of bone and plate cross sections were obtained from the SolidWorks design software, and the centroid of combined cross section was obtained through the application of (5) and (6) expressions.

In next section, the numerical model results are shown.

Table 1 Cross-sectional dimensions

Dimensions (mm)	Bone (Fig. 7b)	Bone (Fig. 7c)	Plate
D_i	15.4	15.4	–
D_o	32.2	31.6	–
d	–	–	4.5
B	–	–	16.5
H	–	–	4.8

Table 2 Plate cross-sectional shifts

Dimensions (mm)	Full (Fig. 8a)	Hollow (Fig. 8b)
m	1.6	0.9
n	−1.3	−1.3
s	−10.9	−10.0
t	9.0	9.9

These dimensions are referred to local coordinates in Fig. 4

Table 3 Isotropic material properties [18]

Material properties	Bone	Plate
Modulus of elasticity (GPa)	20	190
Shear modulus (GPa)	8.1	73
Poisson ratio	0.235	0.3

Table 4 Loading forces and point of application of forces [18]

	Bone
Joint reaction P_1 (N)	(−1062; −130; −2800)
Abductors P_2 (N)	(430; 0; 1160)
Iliopsoas P_3 (N)	(78; 560; 525)
Iliotibial tract P_4 (N)	(0; 0; −1200)
Point of application of joint reaction (mm)	(37.4; −11.1; 218.0)
Point of application of abductors (mm)	(−26.8; −14.9; 200.0)
Point of application of iliopsoas (mm)	(5.5; −37.7; 143.7)
Point of application of iliotibial tract (mm)	(−37.9; −12.6; 168.0)

3.3 Numerical model results

In this section, the results of the numerical model are provided. The results of ANSYS program are shown in Fig. 9 for cross-sectional longitudinal stresses and strains, for both full and hollow plate cross sections.

To estimate which parcel of each material resistance is spent in this example, the resistance characteristics of both materials were accessed. From [17] it was obtained the bone ultimate stress $S_{ut\_bone} = 135$ MPa and from [39] it was obtained the plate yielding resistance $S_{y\_plate} = 690$ MPa. Analyzing Fig. 9a, the plate and bone maximum stresses are, respectively, around 8 % and up to 8 % of their respective resistances, whereas for Fig. 9c, the plate and bone maximum stresses are, respectively, around 9 % and up to 15 % of their respective resistances. In addition, it is interesting to check that the strain patterns have continuity through plate and bone cross sections. Figure 10 shows plate von Mises equivalent stress in different views.

In Fig. 10, the von Mises stress color scale is quite discretized between 0 and 100 MPa, but present only the red color between 100 and 533 MPa. This approach was implemented to show a detailed description over almost all plate surfaces and reserve the red color to represent only few punctual plate regions that hardly can be seen in the figures.

The plate central region and around the internal holes (diaphysis region) are the critical regions. Therefore, the plate central region, the stress distribution has higher values than other plate parts and it can be even more critical during healing process early stages. The von Mises stresses are higher between the internal screws and then decrease almost to zero at external screws (near to the plate ends). Around the holes, the main problem is the contact stresses, which were influenced by the torque applied on the bolts preload. Note that the contact stresses results should be viewed with caution because of its non-linear nature.

Table 5 Equivalent forces/moments at cross-sectional combined centroids

	Plate full/bone (Fig. 8a)	Plate hollow/bone (Fig. 8b)
Cross sections Forces (N)	(609.2; −320.5; −2319)	(609.2; −320.5; −2319)
Cross sections Moments (N m)	(50.2; −4.7; 8.1)	(47.1; 23.2; 8.1)

Table 6 Cross-sectional combined centroids

Dimensions (mm)	Bone	Plate	Combined
Full (Fig. 8a)	(10.9; −1.6; 0)	(−9.0; 1.3; 0)	(0; 0; 0)[a]
Hollow (Fig. 8b)	(10.0; −0.9; −45)	(−10.0; 1.3; −45)	(0; 0; −45)

These dimensions are referred to global coordinates in Fig. 3a

[a] Is the origin of the coordinates

Although Fig. 10 presents a classical way of showing F.E. results, it can be rather difficult to access the stress value of a certain point. To enhance the results sharpness, Fig. 11 shows another way of showing F.E. results: by the utilization of paths. Figure 11a shows a set of plate planes and paths. The planes were divided in five positions: −45, −20, 0, +20, and +45 mm. The plate cross section $z = 0$ mm is at same z axis position of bone cross section in Fig. 6 at position *d*. The −20 and +20 mm planes are at intermediate positions, between the $z = 0$ mm plane and the inner screw holes planes of −45 and +45 mm. Note that planes −20, 0, and +20 mm not have holes and the planes −45 and +45 mm have screw holes are, respectively, at the same *z* axis position of bone cross section in Fig. 6 at positions *e* and *c*.

In Fig. 11a, for −20, 0, and +20 mm planes, there are paths 1, 2, 3, and 4, and for −45 and +45 mm planes and there are paths 1, 2a, 2b, 3, 4a, 4b, 5a, and 5b. These are named transversal paths. Fig. 11b presented

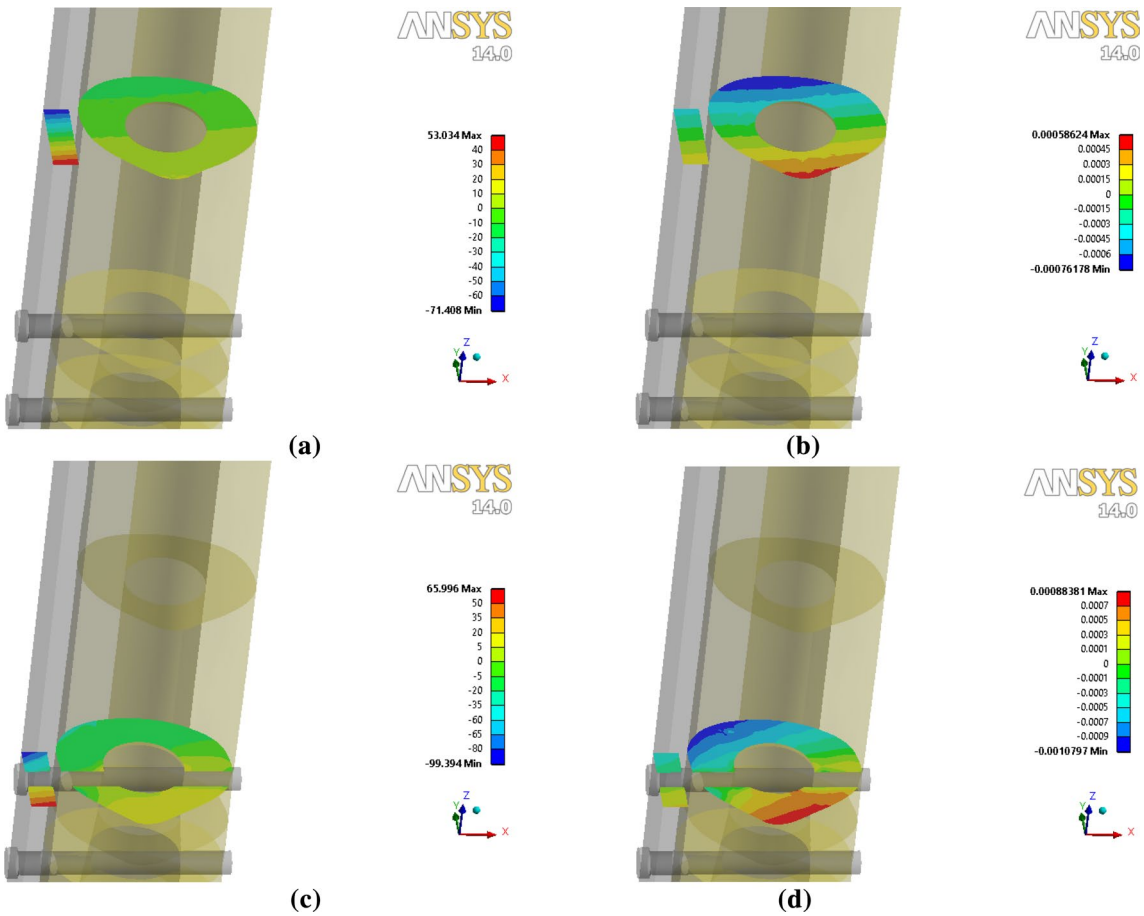

Fig. 9 F.E. results—for full plate cross section: **a** longitudinal normal stress, **b** longitudinal normal strain, and for hollow plate cross section: **c** longitudinal normal stress and **d** longitudinal normal strain

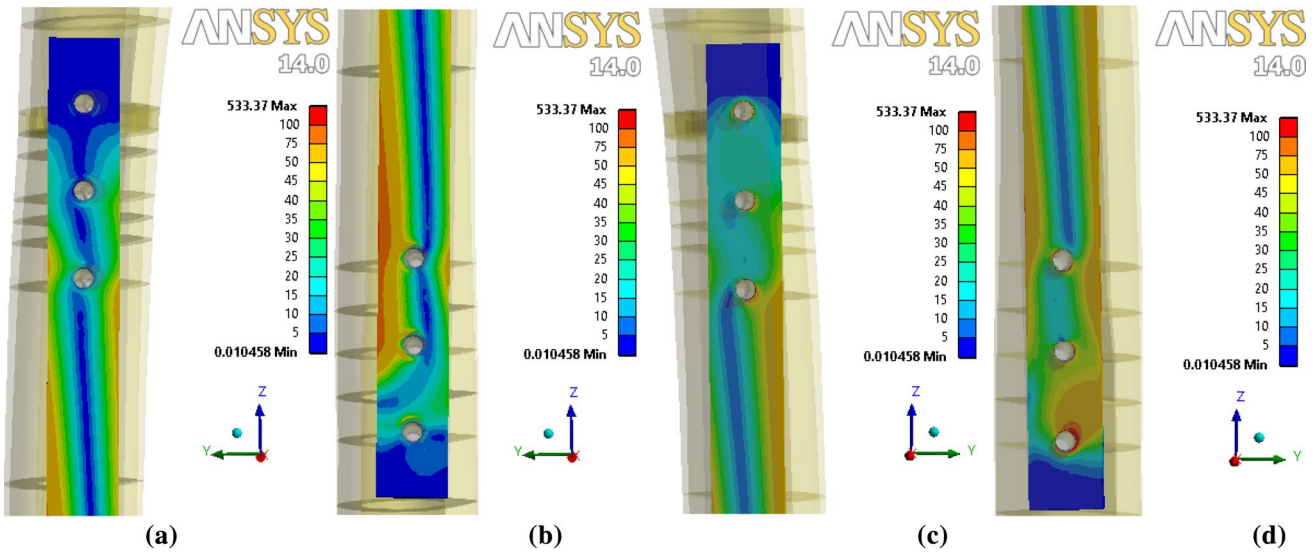

Fig. 10 F.E. results of the von Mises equivalent stress for plate in different views: **a** front/proximal; **b** front/distal; **c** back/proximal; **d** back/distal

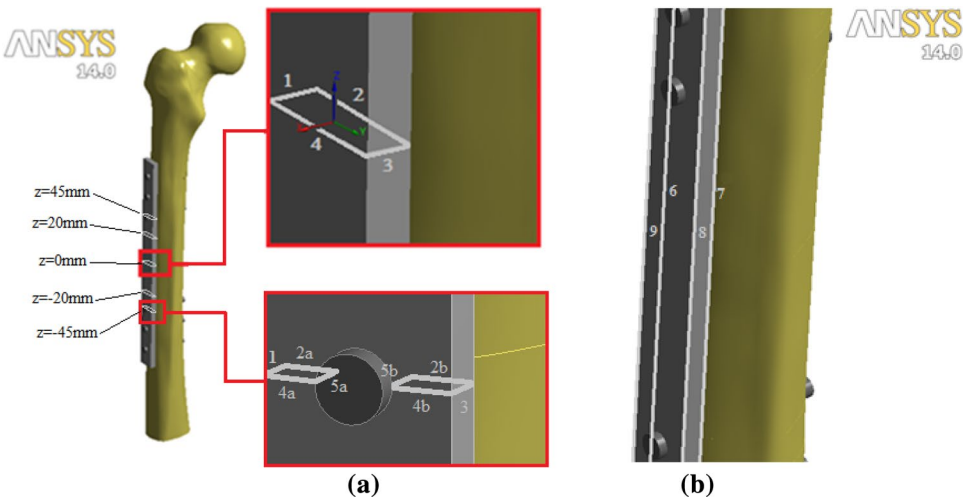

Fig. 11 Paths at plate: **a** transversal paths (for $z = 0$ mm and $z = -45$ mm are detailed) and **b** longitudinal paths

the longitudinal paths 6, 7, 8, and 9 at plate longitudinal edges.

As already commented, the utilization of the classical way of showing F.E. results can lead to difficulties of accessing a certain punctual stress value. Figures 12, 13, and 14 show the F.E. results in a path way. Figure 12 shows von Mises distribution at four horizontal planes ($z = -45$ mm, $z = -20$ mm, $z = +20$ mm, and $z = +45$ mm).

Note that at paths 5a and 5b, along the screw holes, there are stress amplifications only for the plate back region (closer to the bone external surface). Figure 13 shows von Mises distribution at paths 1, 2a, 2b, 3, 4a, and 4b.

Note in Fig. 13, paths 2 and 4 have a significative von Mises Stress variation, in function of bending moment influence around x local axis, as well as the stress concentration influence for the planes with screw holes (-45 and $+45$ mm). Figure 14 shows the longitudinal normal stress variation along the longitudinal paths 6, 7, 8, and 9, the four edges of the plate with respect to the longitudinal coordinate z.

Figure 14 plotted with normal longitudinal stress instead of von Mises equivalent stress used in Figs. 12 and 13, to highlight the edges that are in tension or in compression states. Note that position of the hole screws is represented by dashed horizontal gray lines, where it is possible to see some sharp changes of stress amplitudes. The stresses are the highest at the inner hole screw position (position e in Fig. 6), whereas at the outer hole screws, the longitudinal stresses diminish almost to zero (positions

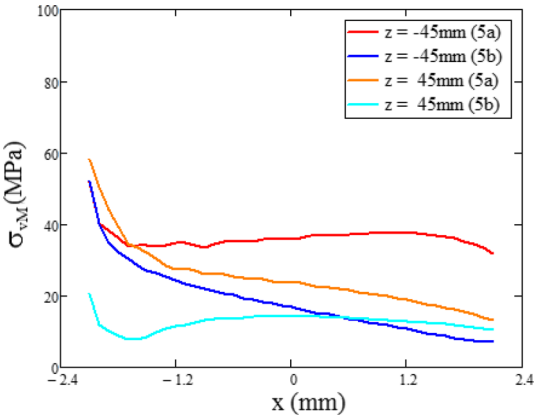

Fig. 12 von Mises stress along paths 5a and 5b

a and *g* in Fig. 6). The cross-sectional result comparisons between analytical and F.E. models, for positions $z = 0$ and $z = -45$ mm (see Fig. 11a), are done at the next item.

4 Results comparison

In this section, the analytical and F.E. model results are presented and compared. The analytical and the F.E. model results for normal longitudinal stresses and for von Mises stresses are presented for two medial cross sections in Fig. 15 (position $z = 0$ mm in Fig. 11a) and Fig. 16 (position $z = -45$ mm in Fig. 11a). To present the analytical results in a similar manner as F.E. postprocessing output, the results of analytical expressions from (1–21) were plotted through the utilization of MATLAB program. As the stresses of the final expressions (20) and (21) are two variable functions, the results could be presented by a Mathlab function using the surf tool, with a color bar to represent the scale. The color scales utilized by analytical and numerical results are the same to allow a direct comparison.

It is important to comment that in addition to the cross-sectional geometric drawbacks of using a simple circular geometry to model the outer bone cross-sectional diameter,

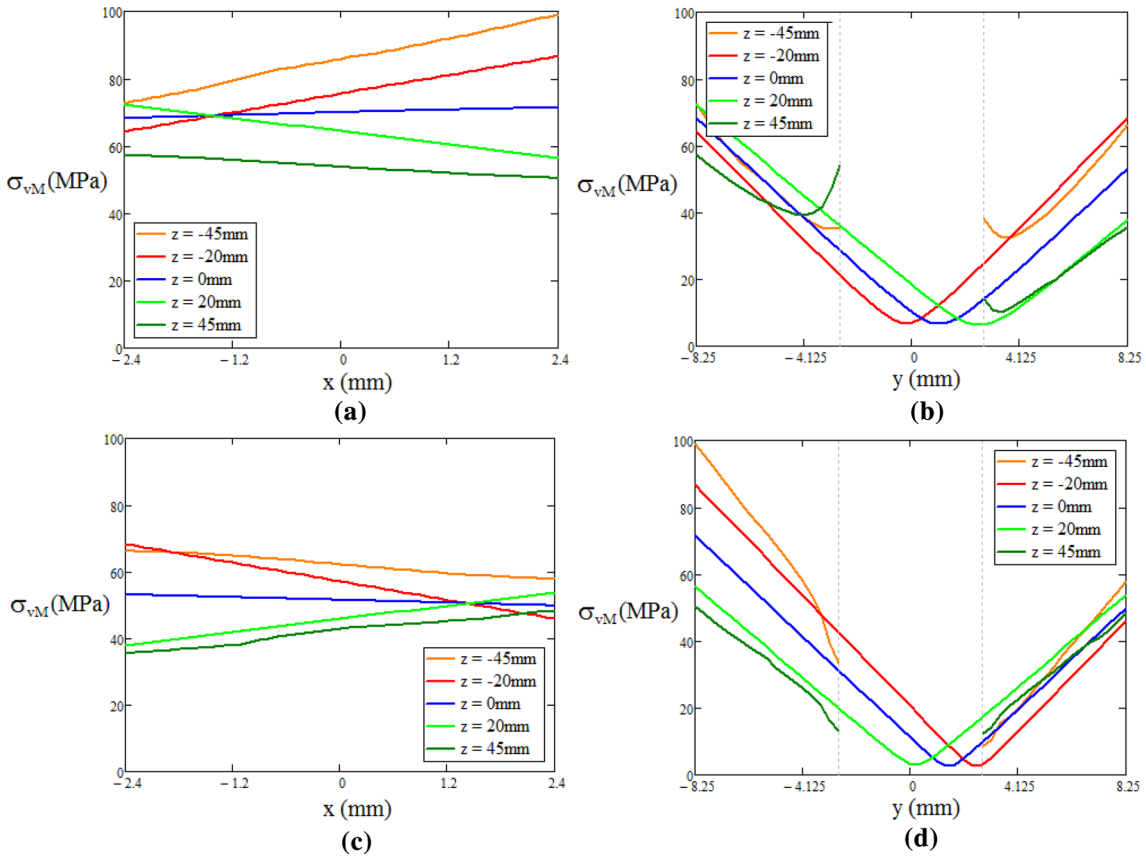

Fig. 13 von Mises stress along: **a** path 1; **b** paths 2, 2a, and 2b; **c** path 3; **d** paths 4, 4a, and 4b

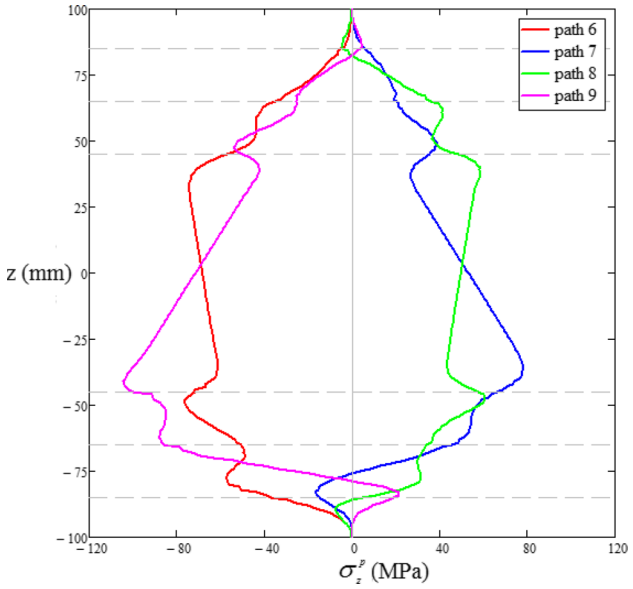

Fig. 14 Normal longitudinal stress along 6, 7, 8, and 9 paths

shown in Fig. 7b and c, there is also the fact that femur bone has a perceptible curvature in both sagital and coronal planes, so the straight plate installation at femur external surface leads to a little deviation from an absolute vertical position. All these errors that summed up can affect the analytical model performance.

5 Conclusions

An analytical model of a bi-material set of a human femur and a plate was implemented using mechanics of solids theory. Every step for the analytical model construction was explicitly presented. The principal steps can be resumed as: from technical literature, it was obtained the forces, at femur head and proximal region, with values, angles, and points of application. In addition, the geometric description of a real human femur bone was obtained. It were estimated the bone, the plate, and the combined cross-sectional centroids at two medial planes bone region; it were establishment equivalent force and moment at combined cross-sectional centroid, a linear transformation for global to local coordinates was set; the calculation of sharing forces and moments between plate and bone cross sections was executed; and the normal stresses (axial and bending) and the shear stresses (transverse and torsion) were estimated. At plate diaphysis cross sections, the normal and shear stresses were summed up through von Mises failure criteria for ductile materials. Finally, the performance of analytical model results was compared to F.E. model results.

Some geometrical details of a real human long bone, as a femur, limited the performance of the analytical model as: the bone cross-sectional outer diameter, that is quite non circular, results in an overall non-constant thickness

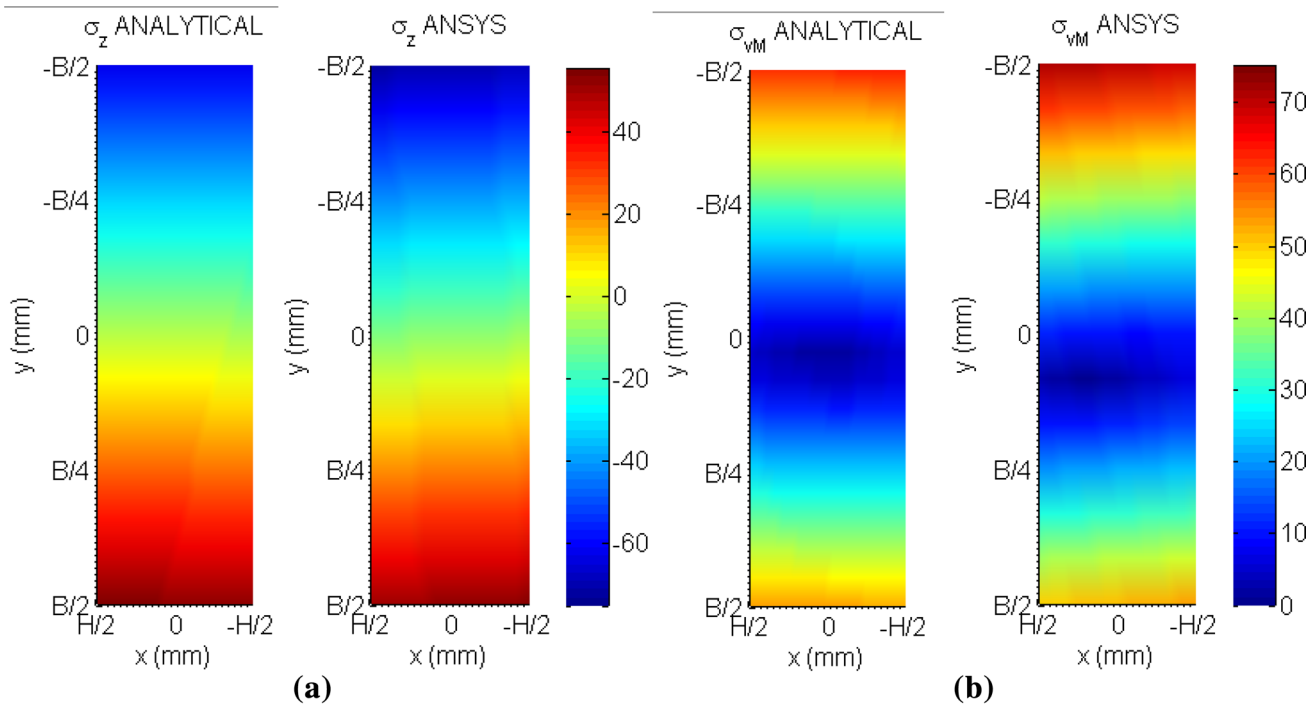

Fig. 15 Cross-sectional stress distribution, at position $z = 0$ mm in Fig. 11a, for analytical and F.E. models: **a** normal longitudinal stresses and **b** von Mises stresses

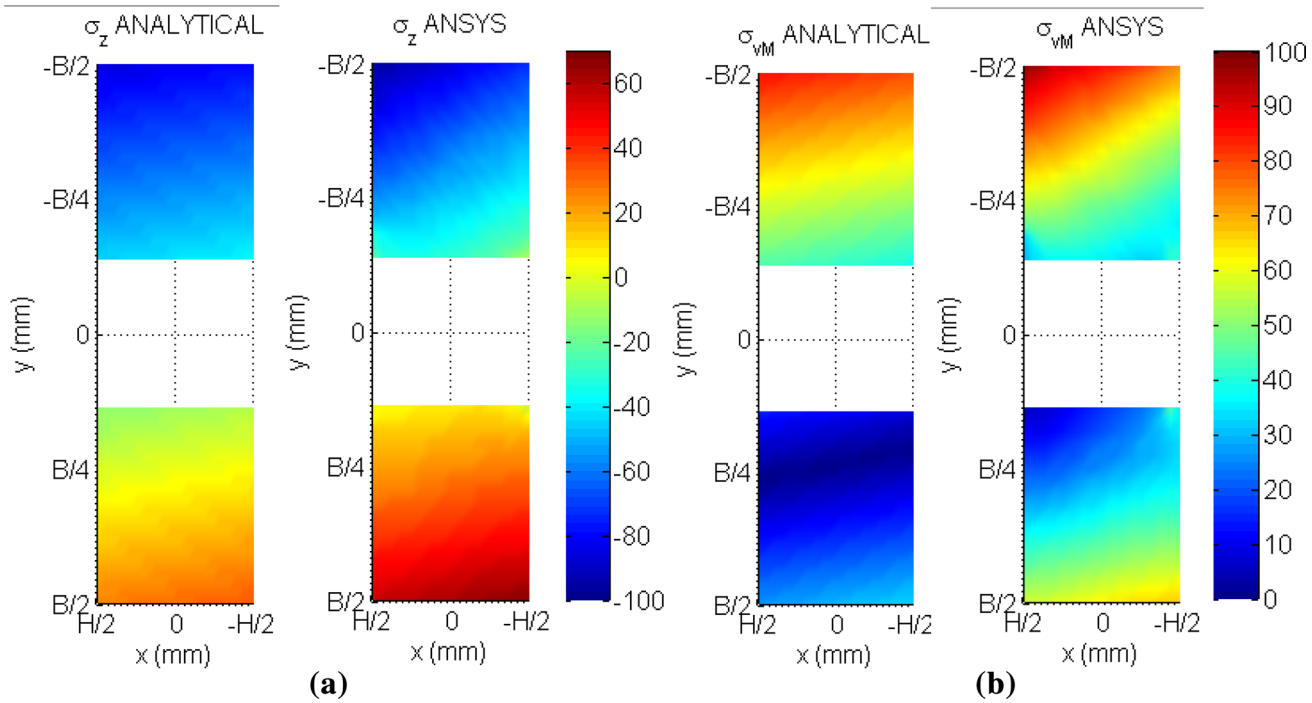

Fig. 16 Cross-sectional stress distribution, at position $z = -45$ mm in Fig. 11a, for analytical and F. E. models: **a** normal longitudinal stresses and **b** von Mises stresses

pattern; the femur bone has a perceptible curvature in both sagital and coronal planes that result in a deviation of plate vertical position after installation, including a significant shift in both x and y local axis directions (transversal directions) with respect to the combined cross-sectional centroid. In addition, some researches use anisotropic constitutive models to describe bone tissue [40].

Because these simplified assumptions, it is expected some inaccuracy of analytical model in comparison with the reference numerical model using the ANSYS, commercial F.E. software. Nevertheless, the utilization of mechanics of solids expressions, with the aid of mathematical software, such as Mathcad or MATLAB, could produce a convincing estimative of a diaphysis plate cross-sectional stress distributions.

Finally, the analytical model estimative of plate cross-sectional stress distribution can be used not only in the design process but also to aid to the stress analysis part of the failure analysis of broken plates, provided that were taking into account the limiting utilization hypothesis and the relative inaccuracy of its results.

Appendix

See Tables 7, 8.

Table 7 Cross-sectional geometric variables

Bone	Plate full	Plate hollow
$A^b = \frac{\pi}{4}\left(D_o^2 - D_i^2\right)$	$A^p = BH$	$A^p = (B-d)H$
$I_x^b = \frac{\pi}{64}\left(D_o^4 - D_i^4\right)$	$I_x^p = \frac{HB^3}{12}$	$I_x^p = \frac{H\left(B^3-d^3\right)}{12}$
$I_y^b = \frac{\pi}{64}\left(D_o^4 - D_i^4\right)$	$I_y^p = \frac{BH^3}{12}$	$I_y^p = \frac{H^3(B-d)}{12}$
–	$Q_x^p(y) = \frac{H}{2}\left[\left(-n+\frac{B}{2}\right)^2 - y^2\right]$	$Q_x^p(y) = \frac{H}{2}\left[\left(-n+\frac{(B-d)}{2}\right)^2 - y^2\right]$
	$for \quad -\frac{B}{2} - n \le y \le \frac{B}{2} - n$	$for \quad -\frac{B}{2} - n \le y \le -\frac{d}{2} - n \quad and \quad \frac{d}{2} - n \le y \le \frac{B}{2} - n$
–	$Q_y^p(x) = \frac{B}{2}\left[\left(\frac{H}{2}+t\right)^2 - x^2\right]$	$Q_y^p(x) = \frac{(B-d)}{2}\left[\left(\frac{H}{2}+t\right)^2 - x^2\right]$
	$for \quad -\frac{H}{2} + t \le x \le \frac{H}{2} + t$	$for \quad -\frac{H}{2} + t \le x \le \frac{H}{2} + t$

Table 8 Aditional expressions

Denomination	Expression
Area ratio	$a^* = \frac{A^p}{A^b}$
Modulus of elasticity ratio	$e^* = \frac{E^p}{E^b}$
Area moment of inertia ratio (relative to axis x)	$s_x^* = \frac{I_x^{p*}}{I_x^{b*}}$
Area moment of inertia ratio (relative to axis y)	$s_y^* = \frac{I_y^{p*}}{I_y^{b*}}$
Rotation transformation matrix around z axis	$\Theta_z = \begin{pmatrix} \cos(\theta_z) & \sin(\theta_z) & 0 \\ -\sin(\theta_z) & \cos(\theta_z) & 0 \\ 0 & 0 & 1 \end{pmatrix}$

References

1. Ahmad M, Nanda R, Bajwa AS, Candal-Couto J, Green S, Hui AC (2007) Biomechanical testing of the locking compressing plate: when does the distance between bone and implant significantly reduce construct stability?, Injury. Int J Care Injured 38:358–364
2. AO Fundation (2013), < https://www2.aofoundation.org/ >
3. Bergmann G, Deuretzbacher G, Heller M, Graichen F, Rohlmann A, Strauss J, Duda GN (2001) Hip contact forces and gait patterns from routine activities. J Biomech 34:859–871
4. Bitsakos C, Kerner J, Fisher I, Amis AA (2005) The effect of muscle loading on the simulation of bone remodelling in the proximal femur. J Biomech 38:133–139
5. Cordey J, Borgeaud M, Perren SM (2000) Force transfer between the plate and the bone: relative importance of the bending stiffness of the screws and the friction between plate and bone. Injury Int J Care Injured 31:21–28
6. Crandall SH, Dahl NC, Lardner TJ (1978) An Introduction to the Mechanics of Solids. Second Edition with SI units, McGraw Hill International Editions
7. Cristofolini L, Viceconti M, Toni A, Giunti A (1995) Influence of Thigh Muscles on the Axial Strains in a Proximal Femur during Early Stance in Gait, Technical Note. J Biomech 28(5):617–624
8. Doblaré M, García JM, Gómez MJ (2004) Modeling bone tissue fracture and healing: a review. Eng Fract Mech 71:1809–1840
9. Duda GN, Heller M, Albinger J, Schulz O, Schneider E, Claes L (1998) Influence of muscle forces on femoral strain distribution. J Biomech 31(9):841–846
10. Duda GN, Schneider E, Chao EYS (1997) Internal Forces and Moments in the Femur during Walking. J Biomech 30(9):933–941
11. Duda GN, Brand D, Freitag S, Lierse W, Schneider E (1996) Variability of femoral muscle attachments. J Biomech 29(9):1185–1190
12. Ecsedi I (2009) Some analytical solutions for Saint-Venant torsion of non-homogeneous cylindrical bars. Eur J Mech A/Solids 28(5):985–990
13. Edwards WB, Gillette JC, Thomas JM, Derrick TR (2008) Internal femoral forces and moments during running: implications for stress fracture development. Clin Biomech 23:1269–1278
14. Frigg, R. (2001) Locking compression plate (LCP). An osteosynthesis plate based on the Dynamic Compression Plate and the Point Contact Fixator (PC-Fix). Injury Int J Care Injured 32:63–66
15. Gdoutos EE, Raftopoulos DD, Baril JD (1982) A Critical Review of the Biomechanical Stress Analysis of the Human Femur. Biomater Rev 3(1):2–8
16. Goswami T, Patel V, Dalstrom DJ, Prayson MJ (2011) Mechanical evaluation of fourth-generation composite femur hybrid locking plate constructs. J Mater Sci Mater Med 22:2139–2146
17. Keaveny TM, Morgan EF, Yeh OC (2004) Standard Handbook of Biomedical Engineering and Design—Chapter 8—Bone Mechanics, Mc Graw Hill Publications
18. Kenedi PP, Riagusoff IIT (2015) Stress development at human femur by muscle forces. J Braz Soc Mech Sci Eng 37(1):31–43
19. Kenedi PP, Vignoli LL (2014) Ostheosynthesis plate: analytical and finite element approaches, XXIV Brazilian Congress of Biomedical Engineering—CBEB 2014, Uberlandia, Brazil
20. Keyak JH, Rosi SA (2000) Prediction of femoral fracture load using finite element models: an examination of stress and strain-based failure theories. J Biomech 33:209–214
21. Kubiak EN, Fulkerson ES, Egol KA (2006) The evolution of locked plates. J Bone Joint Surg Am 88:189–200
22. Lee, H. H. (2002) Finite element simulations with ANSYS workbench 14, SDC Publications
23. Raftopoulos DD, Qassem W (1987) Three-Dimensional Curved Beam Stress Analysis of the Human Femur. J Biomed Eng 9:356–366
24. Ramos A, Simões JA (2006) Tetrahedral versus hexahedral finite elements in numerical modelling of the proximal femur. Med Eng Phys 28:916–924
25. Rockwood G (2006) Fractures in Adults, Chapter 47—fractures of the shaft of the femur, Lippincott Williams & Wilkins, 6th Edition
26. Rudman KE, Aspden RM, Meakin JR (2006) Compression or tension? The stress distribution in the proximal femur, biomedical engineering online 5(12):1–7
27. Simões JA, Vaz MA, Blatcher S, Taylor M (2000) Influence of head constraint and muscle forces on the strain distribution within the intact femur. Med Eng Phys 22:453–459
28. Sokolnikoff IS (1956) Mathematical theory of elasticity, Second Edition, McGraw-Hill Book Company
29. Sommers MB, Fitzpatrick DC, Madey SM, Zanderschulp CV, Bottlang M (2007) A surrogate long-bone model with osteoporotic material properties for biomechanical testing of fracture implants. J Biomech 40:3297–3304
30. Talbot M, Zdero R, Garneau D, Cole PA, Schemitsch EH (2008) Fixation of long bone segmental defects: a biomechanical study. Injury Int J Care Injured 39(2):181–186
31. Taylor ME, Tanner KE, Freeman MAR, Yettram AL (1996) Stress and strain distribution within the intact femur: compression or bending? Med Eng Phys 18(2):122–131
32. Timoshenko S, Goodier JN (1951) Theory of elasticity, Second Edition, McGraw-Hill Book Company
33. Toridis TG (1969) Stress analysis of the femur. J Biomech 2:163–174
34. Tung-Wu Lu, Taylor SJG, O'Connor JJ, Walker PS (1997) Influence of muscle activity on the forces in the femur: an *In Vivo* study. J Biomech 30(11/12):1101–1106
35. Vignoli LL, Kenedi PP (2015) A finite element study of ostheosynthesis plates, V Encontro Nacional de Engenharia Biomecânica—ENEBI 2015, Uberlândia, Brazil
36. Young W, Budynas R (2001) Roark's Formulas for Stress and Strain, Seventh Edition, McGraw-Hill Book Company
37. Pilkey DP, Pilkey DF (2008) Peterson's Stress Concentration Factors, Third Edition, John Wiley and Sons, Inc
38. Glinka G, Newport A (1987) Universal features of elastic notch-tip stress fields. Int J Fatigue (3):143–150
39. International Standard ISO 5832-1 (2007) Implants for surgery—metallic materials—Part 1: Wrought stainless steel, 4th Edition
40. Vignoli LL, Kenedi PP (2016) Stress development at human femur by muscle forces. Lat Am J Solids Struct 13(1):51–72